



Cite this: *Phys. Chem. Chem. Phys.*,  
2020, 22, 18548

# Giant magnetoresistance and dual spin filtering effect in ferromagnetic 6,6,12/ $\gamma$ -graphyne zigzag nanoribbon lateral heterojunction†

Liwen Zhang,<sup>ab</sup> Yaqing Yang,<sup>ab</sup> Jun Chen,<sup>bc</sup> Xiaohong Zheng,<sup>id</sup> \*<sup>ad</sup> Lei Zhang,<sup>id</sup> \*<sup>ab</sup>  
Liantuan Xiao<sup>ab</sup> and Suotang Jia<sup>ab</sup>

Based on non-equilibrium Green's function combined with density functional theory (NEGF-DFT), we investigate the spin dependent transport in the ferromagnetic 6,6,12/ $\gamma$ -graphyne zigzag nanoribbon (GYZNR) heterojunction under different magnetic configurations. It is found that, at low bias [−0.05, 0.1] V, the junction presents metallic transport with negligible spin polarization in parallel configuration (PC) while it behaves as an insulator in anti-parallel configuration (APC), which results in giant magnetoresistance. Interestingly, when we increase the bias voltage beyond [−0.05, 0.1] V, dual spin filtering characterized by electron transport of different spin channels under different polarity of bias is observed in APC but not in PC. All these findings are understood from the symmetry matching of wave functions in two nanoribbons at equilibrium or finite bias. Furthermore, dual spin filtering can also be achieved in PC by applying a gate voltage on the central interface region, which arises from the shift of different single spin channel of the central gate region into the bias window at a different polarity of the gate voltage. Thus, our work demonstrates the great potential of the 6,6,12/ $\gamma$ -GYZNR heterojunction as a multi-functional device and its great perspectives in carbon-based nanoelectronics and spintronics.

Received 21st May 2020,  
Accepted 22nd July 2020

DOI: 10.1039/d0cp02753g

rsc.li/pccp

## 1 Introduction

By utilizing the electron's spin degree of freedom as the information carrier, spintronics is expected to greatly improve the efficiency of data transfer and storage, offering one of the most promising options for future high performance and low energy consumption device.<sup>1–15</sup> At present, a lot of spin-based electronic devices with different functionality, such as, single spin filters, dual spin filters, spin field effect switch and dual spin diodes, have been proposed based on many different materials.<sup>16–24</sup> However, most of them are built by using three dimensional magnetic bulk materials. Due to the requirement of device miniaturization, the design of a spintronic device based on low dimensional materials is becoming more and more popular and important.

More recently, graphyne as a crystalline allotrope of graphene has attracted extensive research attention from both experimental and theoretical sides because of their extraordinary electronic properties.<sup>25–39</sup> Due to the presence of acetylene linkages between neighboring hexagonal rings, there are several different atomic structures in this family such as  $\alpha$ -,  $\beta$ -,  $\gamma$ -,  $\delta$ - and 6,6,12-graphynes.<sup>29,39–41</sup> In these materials, the 6,6,12-graphyne possesses two nonequivalent distorted Dirac cones and its carrier mobility can be largely comparable to graphene.<sup>35,36</sup> The  $\gamma$ -graphyne is the most stable structure among graphyne-*n*.<sup>35</sup> More interestingly, due to the presence of acetylene bonds, graphyne nanoribbons (GYNRs) show different electronic and spintronic properties compared with graphene nanoribbons (GNRs).<sup>24–31,42</sup> It is well known that GNRs have long spin diffusion length and spin relaxation time,<sup>43–45</sup> which makes them potential candidates for many different types of spintronic devices.<sup>22–24,42</sup> Similarly, GYNRs are estimated to have a long spin relaxation time similar to GNRs. Motivated by this, it is speculated that GYNRs should also be useful in the development of a carbon-based spintronic device, for instance, 6,6,12-GYNR and  $\gamma$ -GYNR, which have been extensively studied.<sup>27,30,46–48</sup> Since the interface between two different materials can be commonly used to tune their individual electronic properties, then the following interesting and important questions arise. What if these two different

<sup>a</sup> State Key Laboratory of Quantum Optics and Quantum Optics Devices,  
Institute of Laser Spectroscopy, Shanxi University, Taiyuan 030006, China.  
E-mail: zhanglei@sxu.edu.cn

<sup>b</sup> Collaborative Innovation Center of Extreme Optics, Shanxi University,  
Taiyuan 030006, China

<sup>c</sup> State Key Laboratory of Quantum Optics and Quantum Optics Devices,  
Institute of Theoretical Physics, Shanxi University, Taiyuan 030006, China

<sup>d</sup> Key Laboratory of Materials Physics, Institute of Solid State Physics, HFIPS,  
Chinese Academy of Sciences, Hefei 230031, China.  
E-mail: xzheng@theory.issp.ac.cn

† Electronic supplementary information (ESI) available. See DOI: 10.1039/d0cp02753g

nanoribbons are put in contact? Can spin polarized current or even fully spin polarized current be generated in the lateral heterojunction device? If so, can it be efficiently controlled by the bias or gate voltage applied in the system?

In this work, we answer these questions by investigating the spin-dependent transport properties of a 6,6,12/ $\gamma$ -GYZNR lateral heterojunction from atomic first principle calculations. Based on non-equilibrium Green's function (NEGF) combined with density functional theory (DFT), we find that the perfect dual spin filtering effect within a finite bias voltage region can be achieved in anti-parallel configuration (APC). In contrast, in the same bias voltage region, the spin polarization in parallel configuration (PC) is nearly zero. More importantly, giant magnetoresistance can be obtained when the bias voltage is between  $-0.05$  V and  $0.1$  V. Surprisingly, when a gate voltage  $V_g$  is applied in the interface region in PC, spin polarized current can be generated and hence the spin polarization can be controlled. In particular, the spin polarization in PC can reach  $\sim +100\%$  when  $V_g = -8$  V and  $\sim -100\%$  when  $V_g = 14$  V, respectively. The nearly  $\pm 100\%$  spin polarization region can persist in a wide range of bias voltage. Thus, a dual spin diode device based on the 6,6,12/ $\gamma$ -GYZNR lateral heterojunction regardless of PC or APC can be proposed, which should be a very attractive system in its practical applications in carbon-based nanoelectronic and spintronic devices.

The rest of the paper is organized as follows. In Section 2, the two probe lateral heterojunction device model based on the 6,6,12/ $\gamma$ -GYZNR, the computational details and theoretical formula are presented. The spin-dependent transport properties of the heterojunction device are shown in Section 3. Section 4 serves as the discussion and conclusion part.

## 2 Model and theoretical formalism

The proposed 6,6,12/ $\gamma$ -GYZNR lateral heterojunction is shown in Fig. 1. The whole system can be divided into three parts, *i.e.*, the central scattering region, and the left and right leads which extend to the electron reservoir where the current is collected. As shown in Fig. 1(b), the gate voltage is applied on the interface region (yellow shadow region) in the numerical simulation. Before presenting the spin-dependent transport properties of the lateral heterojunction device, the atomic structures of 6,6,12-GYZNR,  $\gamma$ -GYZNR and their hybrid device are fully relaxed by using the Vienna *ab initio* simulation package (VASP).<sup>49,50</sup> The detailed structural information is presented in the ESI† (Fig. S1 and Table S1). Note that the edges of the nanoribbons are all passivated with hydrogen atoms in order to saturate the dangling bonds.

The spin-dependent transport properties of the 6,6,12/ $\gamma$ -GYZNR lateral heterojunction are investigated by using the NEGF-DFT method,<sup>51</sup> as implemented in the first principles quantum transport package Nanodcal.<sup>51–53</sup> In the self-consistent calculation, the linear combination of atomic orbital (LCAO) basis at the double- $\zeta$  polarization (DZP) level is used to expand the wave function and other physical quantities. The

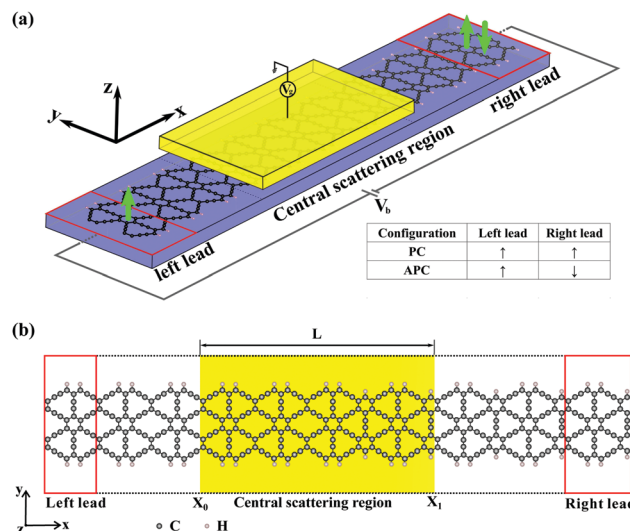


Fig. 1 (a) Schematic plot of the proposed lateral heterojunction device based on hybrid 6,6,12-GYZNR and  $\gamma$ -GYZNR. The red box represents the left/right lead which extends to infinity. The gate voltage is applied on the yellow rectangular area in the central interface region. The green arrows indicate the magnetization of the two leads. The inset table gives out two possible configurations of the system. (b) Top view of the two-probe lateral heterojunction device in the numerical simulation, which can be divided into three parts, the central scattering region, and the left and right leads (red box with solid line). The gate voltage is applied on the interface region between  $X_0$  and  $X_1$  (yellow shadow region) with length  $L = 4.27$  nm. Black and pink balls represent the carbon and hydrogen atoms, respectively.

atomic cores are described by the standard norm-conserving nonlocal pseudo-potentials<sup>54</sup> and the exchange–correlation potential is taken as the generalized gradient approximation (GGA) with the Perdew–Burke–Ernzerhof (PBE) form.<sup>55</sup> The cutoff energy is set to 256 Ry and the first Brillouin zone of the leads is sampled by a  $100 \times 1 \times 1$   $k$ -space grid. The self-consistency is deemed achieved when the monitored quantities such as every element of the Hamiltonian and density matrices differ by less than  $1 \times 10^{-5}$  a.u. between successive iteration steps.

According to the Landauer–Büttiker formula,<sup>56</sup> the spin dependent current  $I^\sigma$  can be calculated with the following formula

$$I^\sigma(V_b) = \frac{e}{h} \int_{-\infty}^{+\infty} T^\sigma(E) [f_L(E, \mu_L) - f_R(E, \mu_R)] dE, \quad (1)$$

where  $e$  and  $h$  are the electron charge and the Planck's constant;  $\mu_{L/R} = E_F \pm \frac{eV_b}{2}$  is the chemical potential in the left/right lead with bias voltage  $V_b$ ;  $f_\alpha(E, \mu_\alpha)$  is the Fermi–Dirac distribution of the  $\alpha$ th lead; the superscript  $\sigma = \uparrow/\downarrow$  denotes the spin up/down component;  $T^\sigma(E) = \text{Tr}[\Gamma_L G^r \Gamma_R G^a]_{\sigma\sigma}$  is the spin dependent transmission coefficient which can be calculated by the standard non-equilibrium Green's function method<sup>51,57</sup> with  $G^{r/a}$  the retarded or advanced Green's function and  $\Gamma_{L/R}$  the linewidth function of the left or right lead.

Furthermore, the spin polarization in PC and APC is defined as

$$SP_{PC/APC}(\%) = \frac{I_{PC/APC}^{\uparrow} - I_{PC/APC}^{\downarrow}}{I_{PC/APC}^{\uparrow} + I_{PC/APC}^{\downarrow}} \times 100. \quad (2)$$

### 3 Results and discussion

To start with, we briefly discuss the electronic structure of the 6,6,12-GYZNR and  $\gamma$ -GYZNR in the ferromagnetic (FM) state with spin magnetic moment  $\mathbf{m} = \uparrow$ . Here, the width of both GYZNRs along the transverse direction is fixed as two unit cell length ( $\sim 1.45$  nm). Because the spin orbital coupling (SOC) effect of GYZNRs are very small (as shown in Fig. S2 in the ESI<sup>†</sup>), it is neglected in our calculation. As shown in Fig. 2, both 6,6,12-GYZNR and  $\gamma$ -GYZNR are in the metallic phase and have large band spin splitting. Through analyzing the wave function of each band around the Fermi level, the symmetry of wave function in each can be classified as  $\pi$  and  $\pi^*$ .<sup>58</sup> When the spin magnetic moment  $\mathbf{m} = \uparrow$ , the spin up bands (red solid lines) are downshifted and the spin down bands (blue solid lines) are upshifted (as shown in Fig. 2(a and b)), which results in an effective magnetic moment  $\mathbf{m}$  of 6,6,12-GYZNR and  $\gamma$ -GYZNR. Compared with 6,6,12-GYZNR, there exist two gap regions with spin up or down bands only ( $[-0.41, -0.31]$  eV for spin up bands and  $[0.3, 0.5]$  eV for spin down bands) in  $\gamma$ -GYZNR (as shown in Fig. S4, ESI<sup>†</sup>). When the spin magnetic moment of 6,6,12 or  $\gamma$ -GYZNR is switched into  $\downarrow$ , the corresponding spin index of each band is also switched but the symmetry of wave function in each band remains the same. This indicates that by contacting two such GYZNRs with the same or different spin magnetic moment, the lateral heterojunction may present fascinating spin and symmetry dependent transport behaviors by utilizing their distinct electronic properties. Moreover, the band structure of the 6,6,12-GYZNR from PBE calculation is compared with that of the HSE06 calculation (as shown in Fig. S3 in the ESI<sup>†</sup>). Around the Fermi level, the band dispersion of both PBE and HSE06 are very similar. Namely, a single

spin up band and a single spin down band cross the Fermi level simultaneously. Most importantly, the symmetries of wave function for these bands calculated by using HSE06 are the same as that of PBE. Our main findings on the giant magnetoresistance and dual spin filtering effect are directly related to the symmetry characteristics of these bands. Since the PBE results can already reflect these characteristics and HSE06 is computationally too expensive, especially for such quantum transport calculations combining density functional theory and non-equilibrium Green's function, we choose PBE instead of using HSE in our numerical simulation.

Having understood the bulk electronic structure of ferromagnetic GYZNRs, we now analyze the electronic transport properties of the lateral heterojunction. As presented in Fig. 1(a), the spin magnetic moment of the left lead (6,6,12-GYZNR) is fixed to up and the right lead ( $\gamma$ -GYZNR) can be either up or down. Thus, two different configurations (listed in the inserted table in Fig. 1(a)) shall be discussed in the following. Firstly, we analyze the equilibrium transport properties of two different configurations. The left columns of Fig. 3(a and b) plot the calculated zero bias transmission  $T^{\sigma}$  in APC and PC, respectively. At first glance, we can see that there are two transmission gap regions for both spin components in APC. One of them is around the Fermi level and another one is below (spin up component) or above (spin down component) the Fermi level. However, there is only one transmission gap region for both spin components in PC. In order to figure out what causes the transmission gap around the Fermi level in APC, we analyze the bandstructure of the spin up component as an example. As shown in the right column of Fig. 3(a and b), the transmission gap region away from the Fermi level (denoted by the green region) is generated due to the existence of an energy gap of spin up in the right lead ( $\gamma$ -GYZNR) as mentioned before.

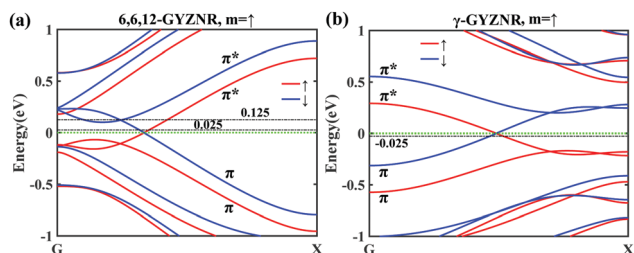


**Fig. 2** (a) Band structure of 6,6,12-GYZNR with spin magnetic moment  $\mathbf{m} = \uparrow$ . (b) Band structure of  $\gamma$ -GYZNR with spin magnetic moment  $\mathbf{m} = \uparrow$ . The red and blue solid lines represent the spin up and spin down component, respectively. The Fermi level is given by the horizontal dashed green line. The black dashed lines represent the corresponding effective electron energy  $E'$  in the non-equilibrium case.  $\pi$  and  $\pi^*$  represent antisymmetric and symmetric states, respectively.

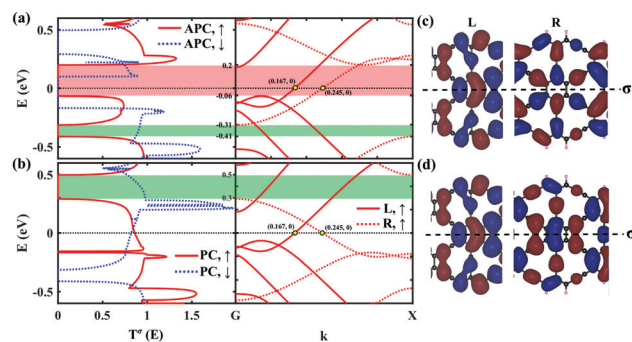


**Fig. 3** Spin dependent transmission coefficients  $T^{\sigma}(E)$  versus energy  $E$  (left column) when  $V_b = 0$  V,  $V_g = 0$  V and band structures (right column) of the spin up component in left and right leads for (a) APC and (b) PC, respectively. The red solid and blue dashed lines (left column) represent the spin up and spin down transmission components, respectively. The red solid and dashed lines (right column) represent band structures of the left and right lead, respectively. The pink and green regions represent transmission gap regions of the spin up component. (c and d) Isosurface plot of the real part of wave functions in the unit cell of the left and right leads when  $E = 0$  eV (denoted by yellow circles in the band structures) in APC and PC, respectively.  $\sigma$  indicates the symmetry axis along the longitudinal direction.

Nevertheless, there are available spin up bands around the Fermi level in the left and right leads in APC. This indicates that there are available DOS for transporting electrons in the system. By further analyzing the wave functions ( $E = 0$  eV) in the unit cell of left and right leads (see Fig. 3(c)) in APC, we found that the wave functions are symmetry mismatching. The wave function in the left lead is symmetric ( $\pi^*$ ) but the wave function in the right lead is antisymmetric ( $\pi$ ), which results in the transmission gap region in APC.<sup>24–26,58–60</sup> In contrast, the wave functions of the left and right leads ( $E = 0$  eV) in PC are both symmetric and matches well, as shown in Fig. 3(d). Thus, the transmissions around the Fermi level in PC are finite. The further detailed transmission coefficients in perfect 6,6-12-GYZNR and  $\gamma$ -GYZNR systems and information on the spin down component of the heterojunction are presented as Fig. S4 and S5 in the ESI.†

Now we focus on the non-equilibrium transport properties of two configurations. Fig. 4(a and b) plots the calculated spin-dependent currents in APC as a function of the bias voltage  $V_b$  ranging from  $-0.2$  V to  $0.2$  V. At a low bias regime ( $V_b \in [-0.05, 0.1]$  V), we see that the generated spin dependent currents are zero and the device is in the off state. As the magnitude of bias voltage further increases, the magnitude of generated spin current can gradually turn on and increases rapidly. Interestingly, we can clearly see that only spin down current is generated in the positive bias regime while the spin up current is nearly completely suppressed in APC. In the negative bias regime, only the spin up current is obtained while the spin down current is nearly completely suppressed. More importantly, the generated current becomes fully spin polarized when the bias voltage approaches  $\pm 0.2$  and the corresponding spin polarization is  $\pm 100\%$ . Physically, the spin up and down currents flow unidirectionally in the counter direction of bias voltage. In this regard, the lateral heterojunction in APC exhibits an excellent dual spin filtering effect. In contrast with APC, the generated current in PC is largely non-spin polarized and is nearly linear in the studied bias region. The corresponding spin polarization is extremely small especially when  $V_b \in [-0.15, 0.2]$  V (see Fig. 4(b)). In the low bias regime ( $V_b \in [-0.05, 0.1]$  V), this lateral heterojunction can be switched on

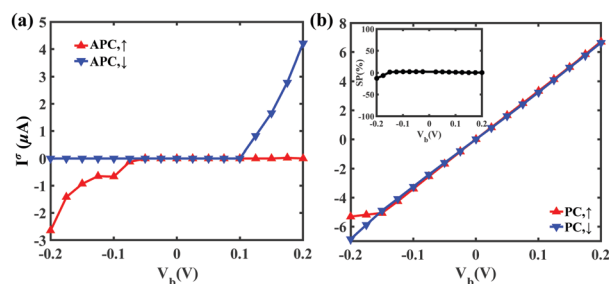


Fig. 4 The spin current  $I^\sigma$  versus the bias voltage  $V_b$  in (a) anti-parallel configuration (APC) and (b) parallel configuration (PC), respectively. The corresponding spin polarizations are shown in the inset. The solid lines with red upper and blue lower triangles represent the spin up ( $\uparrow$ ) and spin down ( $\downarrow$ ) component, respectively.

and off through altering the spin magnetic moment of the right lead, which has a giant magnetoresistance.

To understand the interesting behaviour of current-voltage ( $I$ - $V$ ) characteristics in APC, we examine the spin-dependent transmission coefficients *versus* energy at the non-equilibrium situations. Here, the numerical results of transmission in APC with two typical different bias voltages ( $V_b = \pm 0.15$  V) are shown in the left column of Fig. 5. Due to the Fermi distribution properties in eqn (1), the spin dependent current can be obtained by integrating the non-equilibrium transmission over the corresponding bias window  $[-V_b/2, V_b/2]$  (region enclosed by the horizontal black dashed lines in Fig. 5). We mainly focus on analyzing the transmission coefficients in this region. When  $V_b = 0.15$  V, the spin up transmissions are totally blocked in the bias window but the spin down transmissions become nonzero when  $E$  is between  $0.02$  eV and  $0.075$  eV. This can be understood by analyzing the corresponding bandstructures of two spin components in the left and right leads. Note that the bandstructure of the left and right leads shift down and up according to its corresponding applied bias. In the middle column of Fig. 5(a), the wave functions of the spin up component in the left and right leads are symmetry mismatching ( $\pi^*$  symmetry in the left lead and  $\pi$  in the right lead) in the whole bias window, which results in a transmission gap. Compared with the spin up component, the  $\pi^*$  bands of the spin down component in the left and right leads have some overlap (see the right column of Fig. 5(a)). This is why the spin down transmissions show up in the corresponding region. When  $V_b = -0.15$  V, the situation for two spin components is reversed. From Fig. 5(b), we know that the spin up transmissions are nonzero between  $-0.075$  eV and  $0.01$  eV. However, spin down transmissions are totally blocked in the bias window. Similarly, by analyzing the bandstructure of spin up and down components in Fig. 5(b), we can easily know that the wave functions of spin down bands in the left and right leads are symmetry mismatching resulting in a transmission gap, while

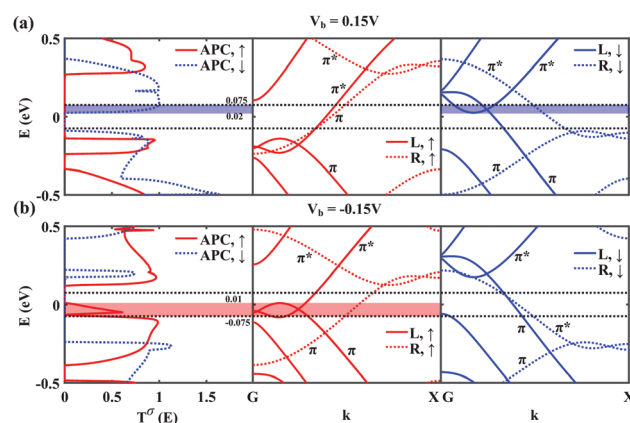


Fig. 5 Spin dependent transmission coefficients  $T^\sigma(E)$  versus energy  $E$  under different bias voltages in APC. (a and b) APC with  $V_b = \pm 0.15$  V, respectively. The red solid line and blue dashed line represents the spin up ( $\uparrow$ ) and spin down ( $\downarrow$ ) component, respectively. The region enclosed by the black dashed lines indicates the bias window.



the spin up bands with  $\pi$  antisymmetry have an overlap region. We conclude that due to the mismatching mechanism of the wave functions, the dual spin filtering effect can be realized in APC.

Can the large spin polarized current be produced in PC? In the following, we shall show that the dual spin filtering effect can also be achieved in PC through applying the gate voltage. Here, the gate voltage is applied in the interface region of the heterojunction as shown in Fig. 1. Fig. 6(a and b) plots the current *versus* the gate voltage and the corresponding spin polarization when the bias voltage is fixed as 0.05 V. At  $V_g = 0$  V, the spin up and down currents are nearly equal to each other and hence the spin polarization is extremely small. By increasing the magnitude of gate voltage  $V_g$ , the difference between spin up and down currents becomes substantially large. When  $V_g < 0$  V, the spin down current decreases rapidly, while the spin up current remains finite, especially when  $V_g$  is around  $-10$  V. As shown in Fig. 6(b), the spin polarization approaches 100%. Correspondingly, the situation is reversed when  $V_g > 0$  V resulting in an  $SP \simeq -100\%$  region. Importantly, we found that the gate voltage can be used to generate nearly unidirectional spin current in positive/negative gate voltage in PC. For instance, when  $V_b = 0.05$  V and  $V_g = -8$  V, the spin up polarization is about 98%. However, when  $V_b = 0.05$  V and  $V_g = 14$  V, the spin down polarization is about  $-95\%$  (as shown in Fig. 6(b)). To confirm the robustness of the interesting gate voltage effect in the PC case, we further calculate the spin

current *versus* the bias voltage when the gate voltage  $V_g$  is fixed as  $-8$  V and  $+14$  V. In Fig. 6(c and d), we see that the spin down current remains nearly flat as zero while the spin up current shows a linear dependence on the bias when  $V_b \in [-0.1, 0.1]$  V and  $V_g = -8$  V. At the same time, the spin polarization remains nearly 100% in this bias region. In turn, when  $V_g = 14$  V, the spin up current is greatly suppressed while the spin down current shows a linear dependence on the bias when  $V_b \in [-0.1, 0.1]$  V, which results in  $SP \simeq -100\%$ .

The interesting dual spin filtering effect in PC may be understood intuitively and approximately by the shift of different single spin channel region in the electronic structure of the central gate region into the bias window at each polarity of the gate voltage. Even though the bandstructure's physical picture is no longer valid for the finite region, the  $\gamma$ -GYZNR in the gate region should have spin dependent gaps as its bulk form (see Fig. 2(b)). By applying the negative gate voltage  $V_g$ , the energy levels of  $\gamma$ -GYZNR in the gate region should shift upward. Once the corresponding spin down energy gap shifts into the bias window region, the spin down channels are greatly reduced, while the transmissions of spin up channels can still be finite values. In contrast, the spin up energy gap can shift into the bias window region when the positive gate voltage is applied. This physical picture is reinforced by investigating the local density of states (LDOS)  $n^\sigma(E, x, y)$  with the different spin components. As shown in Fig. 7(a and b), the averaged LDOS  $\bar{n}^\sigma(E, x)$  when  $V_g = -8$  V and  $V_g = 14$  V have different patterns. When  $V_g = -8$  V, the LDOS  $\bar{n}^1(E, x)$  distribute over the whole gate region but  $\bar{n}^2(E, x)$  are nearly zero in the center of the gate region. On the other hand, when  $V_g = 14$  V, the LDOS  $\bar{n}^1(E, x)$  are nearly zero in the center of the gate region comparing with large  $\bar{n}^2(E, x)$ . Therefore, the local gap is formed for different spin channels depending on the polarity of the gate voltage. Due to the presence of a local gap, the dual spin filtering effect in PC can be produced. Therefore, both the bias and gate voltage are efficient tools to tune the spin polarization of the 6,6,12/ $\gamma$ -GYZNR lateral heterojunction device.

Finally, in order to give a vivid physical picture of the electron transport process in different situations of the lateral heterojunction, we study the scattering states injecting from

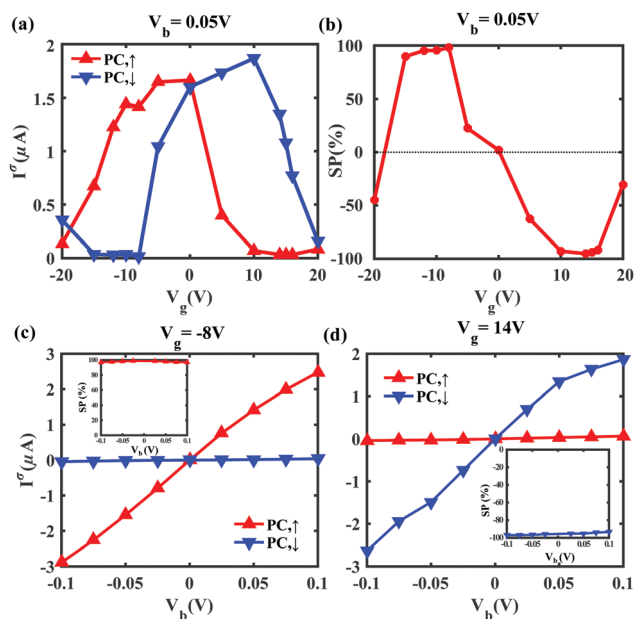


Fig. 6 (a) Spin-dependent current *versus* the gate voltage  $V_g$  when the bias voltage  $V_b = 0.05$  V in PC. The solid lines with red upper and blue lower triangles represent the spin up ( $\uparrow$ ) and spin down ( $\downarrow$ ) current, respectively. (b) The corresponding spin polarization *versus* the gate voltage  $V_g$  when the bias voltage  $V_b = 0.05$  V. (c) Spin-dependent current and corresponding spin polarization *versus* the bias voltage  $V_b$  when the gate voltage  $V_g = -8$  V. (d) Spin-dependent current and corresponding spin polarization *versus* the bias voltage  $V_b$  when the gate voltage  $V_g = 14$  V.

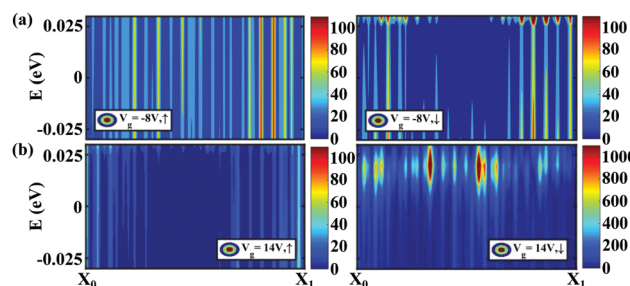
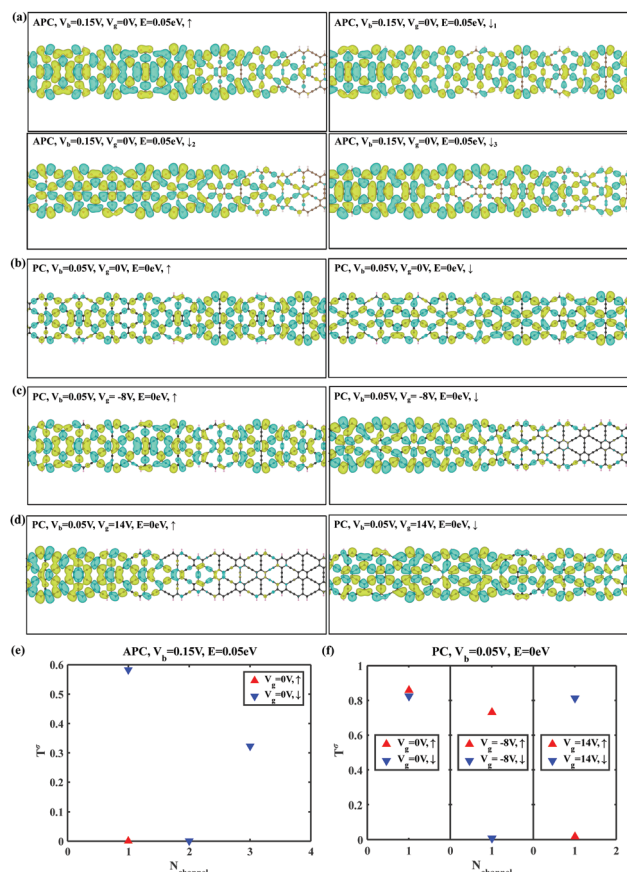


Fig. 7 Local density of states (LDOS)  $\bar{n}^\sigma(E, x)$  with spin component  $\sigma = \uparrow, \downarrow$  averaged over transverse direction  $y$  calculated by  $\bar{n}^\sigma(E, x) = \int n^\sigma(E, x, y) dy$  when energy  $E \in [-V_b/2, V_b/2]$  where  $V_b = 0.05$  V and  $x \in [X_0, X_1]$ . (a) LDOS with spin up and down component when  $V_g = -8$  V. (b) LDOS with spin up and down component when  $V_g = 14$  V.



**Fig. 8** (a–d) Isosurface plot of the real part of the scattering wave functions with spin up/down component in APC ( $V_b = 0.15$  V,  $E = 0.05$  eV) and PC ( $V_b = 0.05$  V,  $V_g = 0, -8, 14$  V,  $E = 0$  eV) correspondingly. (e and f) The spin dependent transmission  $T^\sigma$  of the corresponding channels in APC ( $V_b = 0.15$  V) and PC ( $V_b = 0.05$  V,  $V_g = 0, -8, 14$  V), respectively.

6,6,12-GYZNR (left lead) and transporting through the central scattering region. Without the loss of generality, the scattering wave functions when electron energy ( $E$ ) is equal to 0.05 eV and  $V_b = 0.15$  V in APC and electron energy ( $E$ ) is equal to 0 and  $V_b = 0.05$  V in PC are selected as an example. Fig. 8(a) shows the isosurface of the real part of scattering states distribution in APC. Since the bias voltage applied in the left lead of 6,6,12-GYZNR is  $eV_b/2 = 0.075$  eV, the actual injecting electron energy is  $E' = eV_b/2 + E = 0.125$  eV. From the bandstructure of 6,6,12-GYZNR (left lead) as shown in Fig. 2(a), we can know that there are one spin up state ( $\pi^*$  symmetric) and three spin down states (one  $\pi$  antisymmetric and two  $\pi^*$  symmetric) when  $E' = 0.125$  eV. In Fig. 8(a), we can clearly see that the  $\pi^*$  symmetric spin up state is totally blocked while the first and third spin down channels can partially go through the device. Note that the corresponding transmission coefficients of each channel are given in Fig. 8(e). Physically, the corresponding states in the  $\gamma$ -GYZNR right lead is  $\pi$  antisymmetric when the effect energy  $E' = -eV_b/2 + E = -0.025$  eV. Due to the mismatch of the symmetry of the injecting and outgoing states in the left and right leads, the injecting spin up state is blocked, *i.e.*, the injecting state is  $\pi^*$  symmetric but the outgoing state is  $\pi$  antisymmetric. Thus, only

spin down current can be generated in the positive bias region as shown in Fig. 4(a). Similarly, the spin up current generated in the negative bias region can also be understood (as shown in Fig. S6, ESI†). In general, the spin dependent transmission gap generated in APC can be understood in a similar way. For the scattering states in PC when  $V_g = 0$ , the effective energy of injecting states in 6,6,12-GYZNR is  $E' = eV_b/2 + E = 0.025$  eV. The corresponding spin up and down states are  $\pi^*/\pi$  symmetric as shown in Fig. 2(a). In  $\gamma$ -GYZNR (right lead), the corresponding outgoing spin up/down states [ $E' = -eV_b/2 + E = -0.025$  eV] with the same symmetry ( $\pi^*/\pi$ ) states both exist (see Fig. 2(b)). Then the spin up and down states can largely go through the interface region without much reflection (see the transmission coefficients in the first panel in Fig. 8(f)). At this time, the wave functions match well. Furthermore, when the gate voltage  $V_g$  is turned to  $-8$  V and  $14$  V in PC, the gate voltage can shift the energy levels of  $\gamma$ -GYZNR in the interface region resulting in a local spin dependent energy gap. Therefore, physically speaking, the gate voltage in PC can play a role of the spin filter. From Fig. 8(c and d), it is clear that the spin down ( $\pi$ ) or up channel ( $\pi^*$ ) is nearly blocked (see the corresponding transmission coefficient in the second and third panels in Fig. 8(f)), respectively. Thus the dual spin filtering effect can be achieved in the opposite gate voltages in PC.

## 4 Conclusions

In summary, we theoretically investigated the spin-dependent transport properties of the 6,6,12/ $\gamma$ -GYZNR lateral heterojunction from atomic first principles. By calculating the spin dependent current in both PC and APC, we found that the perfect dual spin filtering effect can be easily obtained in APC within a certain bias voltage range. However, for PC, the spin polarization is nearly zero within the same bias voltage range. In the low bias voltage regime, giant magnetoresistance can be obtained. Through applying the gate voltage in the interface region of the lateral heterojunction, the dual spin filtering effect is also achieved in PC. Even more importantly, when the gate voltage  $V_g$  is fixed as  $-8/14$  V, the nearly  $\pm 100\%$  spin polarization can be obtained within the bias voltage range  $[-0.1, 0.1]$  V, respectively. Our numerical findings indicate that the 6,6,12/ $\gamma$ -GYZNR lateral heterojunction can be functionalized as a potential nanoelectronic and spintronic device.

## Conflicts of interest

There are no conflicts to declare.

## Acknowledgements

We also gratefully acknowledge the support from the National Natural Science Foundation of China (Grants No. 11704232, 11674204, 11974355, 11574318), the National Key R&D Program of China under Grants No. 2017YFA0304203, PCSIRT (No. IRT\_17R70), 1331KSC, the Shanxi Province 100-Plan Talent Program, and the Program of State Key Laboratory of Quantum

Optics and Quantum Optics Devices (No. KF201810). This research was conducted using the High Performance Computer of Shanxi University.

## References

- 1 S. A. Wolf, D. D. Awschalom, R. A. Buhrman, J. M. Daughton, S. von Molnár, M. L. Roukes, A. Y. Chtchelkanova and D. M. Treger, *Science*, 2001, **294**, 1488–1495.
- 2 A. Dankert and S. P. Dash, *Nat. Commun.*, 2017, **8**, 16093.
- 3 S. Ganichev, E. Ivchenko, V. Bel'kov, S. Tarasenko, M. Sollinger, D. Weiss, W. Wegscheider and W. Prettl, *Nature*, 2002, **417**, 153–156.
- 4 P. Jiang, X. Tao, H. Hao, L. Song, X. Zheng, L. Zhang and Z. Zeng, *2D Mater.*, 2017, **4**, 035001.
- 5 B. Wang, J. Li, Y. Yu, Y. Wei, J. Wang and H. Guo, *Nanoscale*, 2016, **8**, 3432–3438.
- 6 G. Tang, F. Xu, S. Mi and J. Wang, *Phys. Rev. B*, 2018, **97**, 165407.
- 7 M. Oltcher, F. Eberle, T. Kuczmik, A. Bayer, D. Schuh, D. Bougeard, M. Ciorga and D. Weiss, *Nat. Commun.*, 2017, **8**, 1807.
- 8 B. Behin-Aein, D. Datta, S. Salahuddin and S. Datta, *Nat. Nanotechnol.*, 2010, **5**, 266–270.
- 9 L. Tao, K. Cheung, L. Zhang and J. Wang, *Phys. Rev. B*, 2017, **95**, 121407.
- 10 I. Žutić, J. Fabian and S. D. Sarma, *Rev. Mod. Phys.*, 2004, **76**, 323.
- 11 J. Li, B. Wang, F. Xu, Y. Wei and J. Wang, *Phys. Rev. B*, 2016, **93**, 195426.
- 12 M.-M. Wei, Y.-T. Zhang, A.-M. Guo, J.-J. Liu, Y. Xing and Q.-F. Sun, *Phys. Rev. B*, 2016, **93**, 245432.
- 13 M. Gurram, S. Omar and B. J. van Wees, *2D Mater.*, 2018, **5**, 032004.
- 14 A. Fert, *Rev. Mod. Phys.*, 2008, **80**, 1517–1530.
- 15 S. Datta and B. Das, *Appl. Phys. Lett.*, 1990, **56**, 665–667.
- 16 K. Gong, L. Zhang, D. Liu, L. Liu, Y. Zhu, Y. Zhao and H. Guo, *Nanotechnology*, 2014, **25**, 435201.
- 17 Y. J. Dong, X. F. Wang, S. W. Yang and X. M. Wu, *Sci. Rep.*, 2014, **4**, 6157.
- 18 J. Li, G. Gao, Y. Min and K. Yao, *Phys. Chem. Chem. Phys.*, 2016, **18**, 28018–28023.
- 19 E. G. Marin, D. Marian, G. Iannaccone and G. Fiori, *Phys. Rev. Appl.*, 2018, **10**, 044063.
- 20 M. E. Flatté and G. Vignale, *Appl. Phys. Lett.*, 2001, **78**, 1273–1275.
- 21 C. A. Merchant and M. Nina, *Phys. Rev. Lett.*, 2008, **100**, 156601.
- 22 M. Zeng, L. Shen, M. Zhou, C. Zhang and Y. Feng, *Phys. Rev. B: Condens. Matter Mater. Phys.*, 2011, **83**, 5121–5124.
- 23 W. Yan, O. Txoperena, R. Llopis, H. Dery, L. E. Hueso and F. Casanova, *Nat. Commun.*, 2016, **7**, 13372.
- 24 T. Ozaki, K. Nishio, H. Weng and H. Kino, *Phys. Rev. B: Condens. Matter Mater. Phys.*, 2010, **81**, 075422.
- 25 Y. H. Zhou, J. Zeng and K. Q. Chen, *Carbon*, 2014, **76**, 175–182.
- 26 Y. Ni, X. Wang, W. Tao, S. C. Zhu and K. L. Yao, *Sci. Rep.*, 2016, **6**, 25914.
- 27 C. C. Zhao, S. H. Tan, Y. H. Zhou, R. J. Wang, X. J. Wang and K. Q. Chen, *Carbon*, 2017, **113**, 170–175.
- 28 Y. Ni, K.-L. Yao, H.-H. Fu, G.-Y. Gao, S.-C. Zhu, B. Luo, S.-L. Wang and R.-X. Li, *Nanoscale*, 2013, **5**, 4468–4475.
- 29 X. Li, L. Cao, M. Long, Z. Liu and G. Zhou, *Carbon*, 2018, **131**, 160–167.
- 30 L. Cao, X. Li, C. Jia, G. Liu, Z. Liu and G. Zhou, *Carbon*, 2018, **127**, 519–526.
- 31 W. Wu, W. Guo and C. Z. Xiao, *Nanoscale*, 2013, **5**, 9264–9276.
- 32 T. Lin and J. Wang, *ACS Appl. Mater. Interfaces*, 2019, **11**, 2638–2646.
- 33 C. Ge, J. Chen, S. Tang, Y. Du and N. Tang, *ACS Appl. Mater. Interfaces*, 2019, **11**, 2707–2716.
- 34 J. Chen, J. Xi, D. Wang and Z. Shuai, *J. Phys. Chem. Lett.*, 2013, **4**, 1443–1448.
- 35 J. Kang, Z. Wei and J. Li, *ACS Appl. Mater. Interfaces*, 2019, **11**, 2692–2706.
- 36 D. Malko, C. Neiss, F. Viñes and A. Görling, *Phys. Rev. Lett.*, 2012, **108**, 086804.
- 37 Z. Li, M. Smeu, A. Rives, V. Maraval, R. Chauvin, M. A. Ratner and E. Borguet, *Nat. Commun.*, 2015, **6**, 6321.
- 38 L. Jin, L. C. Xu, Y. Yang, X. Liu and Y. Zhi, *Carbon*, 2018, **132**, 632–640.
- 39 A. Saraiva-Souza, M. Smeu, L. Zhang, M. A. Ratner and H. Guo, *J. Phys. Chem. C*, 2016, **120**, 4605–4611.
- 40 G. Yu, Z. Liu, W. Gao and Y. Zheng, *J. Phys.: Condens. Matter*, 2013, **25**, 285502.
- 41 M. Zhao, W. Dong and A. Wang, *Sci. Rep.*, 2013, **3**, 3532.
- 42 S. Lakshmi, S. Roche and G. Cuniberti, *Phys. Rev. B: Condens. Matter Mater. Phys.*, 2009, **80**, 2665–2668.
- 43 O. V. Yazyev, *Nano Lett.*, 2008, **8**, 1011–1015.
- 44 O. V. Yazyev and M. I. Katsnelson, *Phys. Rev. Lett.*, 2008, **100**, 047209.
- 45 G. Cantele, Y.-S. Lee, D. Ninno and N. Marzari, *Nano Lett.*, 2009, **9**, 3425–3429.
- 46 J. Li, Z. Yang, L.-C. Xu, Y. Yang and X. Liu, *J. Mater. Chem. C*, 2019, **7**, 1359–1369.
- 47 D.-D. Wu, Q.-B. Liu, H.-H. Fu and R. Wu, *Nanoscale*, 2017, **9**, 18334–18342.
- 48 X. Cui, T. Ouyang, J. Li, C. He, C. Tang and J. Zhong, *Phys. Chem. Chem. Phys.*, 2018, **20**, 7173–7179.
- 49 G. Kresse and J. Furthmüller, *Phys. Rev. B: Condens. Matter Mater. Phys.*, 1996, **54**, 11169–11186.
- 50 G. Kresse and J. Hafner, *Phys. Rev. B: Condens. Matter Mater. Phys.*, 1993, **47**, 558–561.
- 51 J. Taylor, H. Guo and J. Wang, *Phys. Rev. B: Condens. Matter Mater. Phys.*, 2001, **63**, 245407.
- 52 For details of the NanoDcal quantum transport package, see, <http://www.hzwtech.com>.
- 53 L. Zhang, K. Gong, J. Chen, L. Liu, Y. Zhu, D. Xiao and H. Guo, *Phys. Rev. B: Condens. Matter Mater. Phys.*, 2014, **90**, 195428.
- 54 L. Kleinman and D. Bylander, *Phys. Rev. Lett.*, 1982, **48**, 1425.

- 55 J. P. Perdew, K. Burke and M. Ernzerhof, *Phys. Rev. Lett.*, 1996, **77**, 3865.
- 56 M. Büttiker, Y. Imry, R. Landauer and S. Pinhas, *Phys. Rev. B: Condens. Matter Mater. Phys.*, 1985, **31**, 6207–6215.
- 57 D. Waldron, P. Haney, B. Larade, A. MacDonald and H. Guo, *Phys. Rev. Lett.*, 2006, **96**, 166804.
- 58 X. Zheng, J. Lan, X. Wang, L. Huang, H. Hao and Z. Zeng, *Appl. Phys. Lett.*, 2012, **101**, 053101.
- 59 Q. Yue, S. Chang, J. Tan, S. Qin, J. Kang and J. Li, *Phys. Rev. B: Condens. Matter Mater. Phys.*, 2012, **86**, 235448.
- 60 M.-X. Zhai, X.-F. Wang, P. Vasilopoulos, Y.-S. Liu, Y.-J. Dong, L. Zhou, Y.-J. Jiang and W.-L. You, *Nanoscale*, 2014, **6**, 11121–11129.